Journal of Constructional Steel Research 136 (2017) 128–139

Contents lists available at ScienceDirect

Journal of Constructional Steel Research

journal homepage: www.elsevier.com/locate/jcsr

Seismic performance of steel plate slit-friction hybrid dampers

Joonho Lee[1], Hyungoo Kang[2], Jinkoo Kim*

Dept. of Civil and Architectural Engineering, Sungkyunkwan University, Suwon, Republic of Korea

A R T I C L E I N F O

Keywords:
Slit dampers
Friction dampers
Hybrid dampers
Seismic retrofit
Seismic fragility

A B S T R A C T

In this study a new hybrid energy dissipation device is developed by combining a steel slit damper and rotational friction dampers in parallel to be used for seismic retrofit of structures. Compared with the conventional slit dampers with the same yield strength, the hybrid damper has an advantage in that only friction dampers are activated for small earthquakes or strong wind, and both friction and slit damper work simultaneously for strong earthquakes. Cyclic loading tests of the friction, slit, and the combined hybrid dampers are carried out to evaluate their seismic energy dissipation capability. Finite element analyses of the test specimens are also carried out for comparison, which correspond well with the test results. The hybrid dampers are applied to seismic retrofit of an reinforced concrete analysis model structure, where it is observed that the dampers are effective in restraining the building performance within a given target performance level. The fragility analysis of the structure shows that the probabilities of reaching four limit states decrease significantly after the seismic retrofit. The effect is most significant in the reduction of the probability of reaching the complete damage state.

1. Introduction

After the Northridge earthquake in 1994 and Kobe earthquake in 1995, it was observed in many structures that, even though the collapse prevention or the life safety design objective was satisfied, significant economic loss occurred due to major damage in non-structural elements and minor damage in structural elements. To mitigate earthquake induced structural damage, various energy dissipation devices have been applied to structures. Currently two of the most widely used seismic energy dissipation devices in building structures are metallic yield dampers and friction dampers. The metallic energy dissipative devices have been developed in many forms such as ADAS [1], buckling restrained braces [2], and slit dampers [3,4]. Hu [5] investigated the effect of the slit damper made of shape memory alloy. Mualla and Belev [6] developed a rotational friction damper and showed that the hysteretic behavior of the friction damper was frequency-independent. Kim et al. [7] investigated the effect of rotational friction dampers on enhancing seismic and progressive collapse resisting capacity of structures. Patel and Jangid [8] investigated the dynamic response of adjacent structures connected by friction dampers. Kaur et al. [9] compared the seismic performance of a steel moment resisting frame with friction dampers with those of a moment frame and a braced frame. Recently Lee et al. [10] developed friction dampers utilizing friction between low-steel composite material and milled steel, and Kim and Kim [11] developed a seismic retrofit scheme for staggered truss frames using friction dampers.

Attempts have been made to utilize combined mechanism of multiple dampers. Pong et al. [12] investigated the seismic performance of TPEA (tapered-plate energy absorber) combined with fluid dampers or viscoelastic dampers. Uetani et al. [13] applied the gradient projection algorithm for optimum design of a real building structure with viscous and hysteretic dampers. Marshall and Charney [14] studied the concept of the hybrid passive control system with BRB and viscous fluid device by investigating the seismic response of steel frame structures. Murakami et al. [15] proposed a sensitivity-based practical optimization method for simultaneous use of viscous, hysteretic, and inertial mass dampers for earthquakes. Asadi et al. [16] developed a hybrid damper composed of viscous and electromagnetic subsystems, and Wang et al. [17] investigated the effect of tuned mass damper and viscous damper on the mitigation of wind-induced vibration in tall buildings. Lee and Kim [18] investigated the seismic energy dissipation capacity of a hybrid passive damper composed of a friction and a hysteretic slit damper, and compared the results with those of slit and friction dampers with the same yield strength. Kim and Shin [19] carried out seismic loss assessment of a structure retrofitted with slit-friction hybrid dampers, and found that the life cycle cost of a structure with the hybrid dampers is smaller than that of the structure with slit dampers with the same yield strength.

* Corresponding author.
E-mail addresses: jjoonnoo@nate.com (J. Lee), jkim12@skku.edu (J. Kim).
[1] Head of research department, METRO T & C.
[2] Post-doctoral researcher.

http://dx.doi.org/10.1016/j.jcsr.2017.05.005
Received 21 October 2016; Received in revised form 25 April 2017; Accepted 10 May 2017

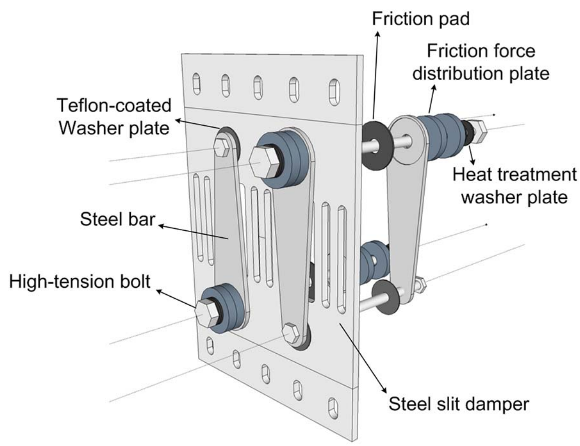

Fig. 1. Hybrid slit-friction damper.

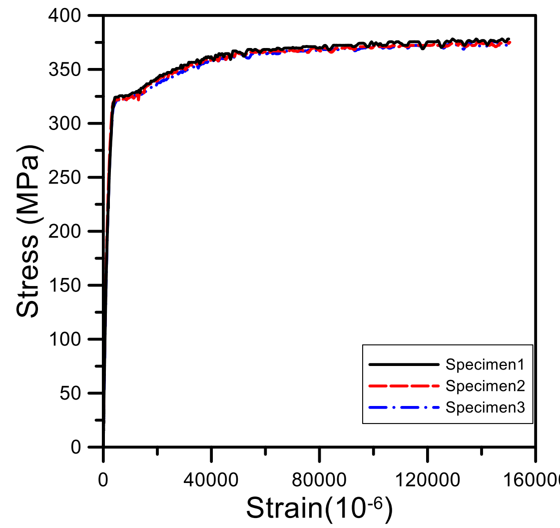

Fig. 3. Stress-strain curve of the steel.

The purpose of this study is to develop a hybrid damper which works for both major and minor earthquakes. To this end the hybrid damper is made of a steel slit damper and rotational friction dampers connected in parallel. For minor earthquakes or strong winds, the slit damper remain elastic and only the friction damper yields to dissipate vibration energy, while for strong earthquakes both the friction and slit dampers work simultaneously to dissipate seismic input energy. Compared with the conventional slit dampers with the same yield strength, the hybrid damper has an advantage in that only friction dampers are activated for small earthquakes or strong wind, and both friction and slit damper work simultaneously for strong earthquakes. Compared with friction dampers the hybrid dampers can be made smaller in size with the same energy dissipation capacity. Cyclic loading tests of the friction, slit, and the combined hybrid dampers are carried out to evaluate their seismic energy dissipation capability, and the results are compared with the finite element analysis results of the test specimens. The hybrid dampers are applied to seismic retrofit of a reinforced concrete analysis model structure, and the effectiveness of the dampers are checked by nonlinear dynamic analyses using the seven earthquake records scaled to the design spectrum. Fragility analyses of the model structure before and after retrofit are also carried out to compare the probability of reaching damage limit states.

2. Analytical modeling of hybrid slit-friction dampers

A steel plate slit damper is composed of many vertical strips as shown in Fig. 1. Based on the assumption that each strip in the slit damper has fixed end condition, the stiffness and the yield strength of a slit damper can be derived as follows [3]:

$$k_s = n\frac{12EI}{l_o^3} = n\frac{Etb^3}{l_o^3} \tag{1a}$$

$$P_{ys} = \frac{2nM_p}{l_0} = \frac{n\,\sigma_y\,tb^2}{2l_0} \tag{1b}$$

where n = number of strips, t = thickness of strips, b = width of strips, and l_o = length of the vertical strip. A friction damper is activated when the applied load reaches the slip force. As the initial stiffness of a friction damper is very large, larger energy is dissipated compared with hysteretic dampers with similar yield force. The yield force of a rotational friction damper can be obtained as follows [20]:

$$P_{yf} = 2\mu\, NQ\,\frac{R_m}{L_0} \tag{2}$$

where L_0 is the length between the two slip pads, μ is the friction coefficient of the friction pad, N is the number of friction face, Q is the clamping force, and R_m is the effective area of the friction face. In case the slit damper and the friction damper are connected in parallel as shown in Fig. 1, the yield strength of the hybrid damper can be obtained as follows:

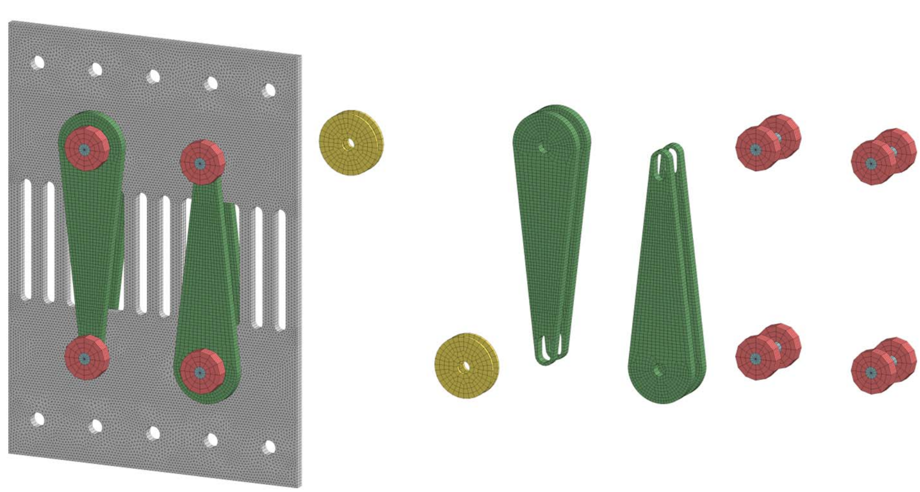

Fig. 2. Finite element model of all components of the hybrid damper.

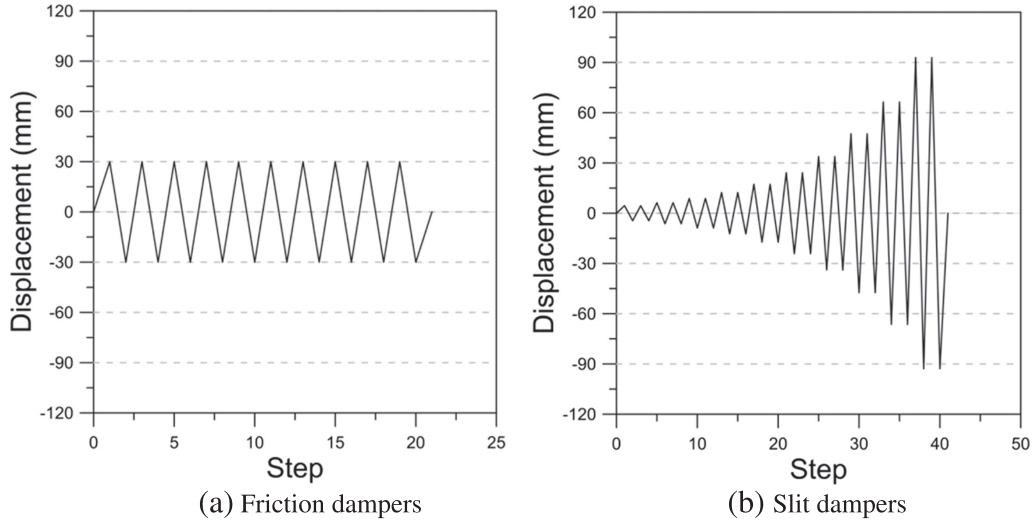

Fig. 4. Loading protocols used in the experiments.

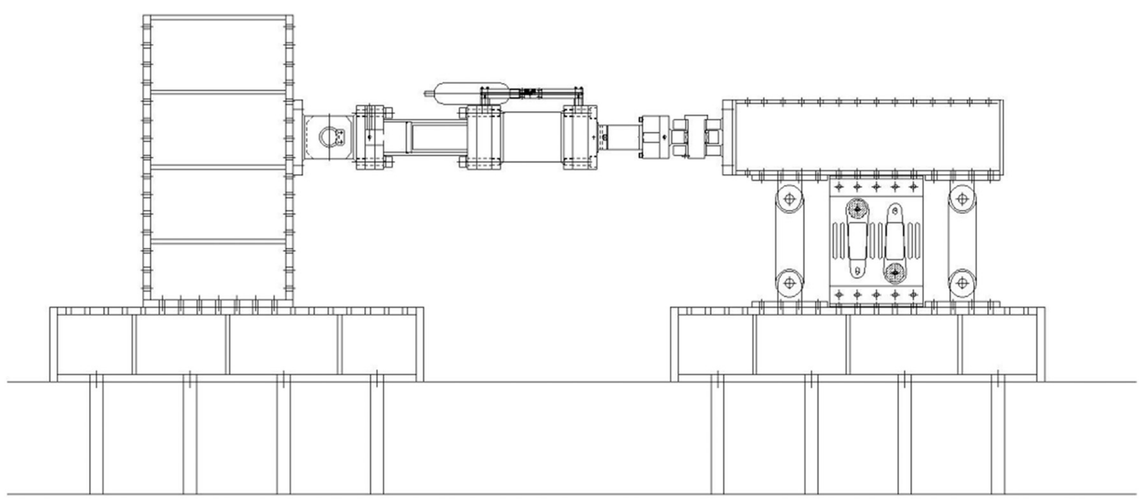

Fig. 5. Test setup for loading test of the specimens.

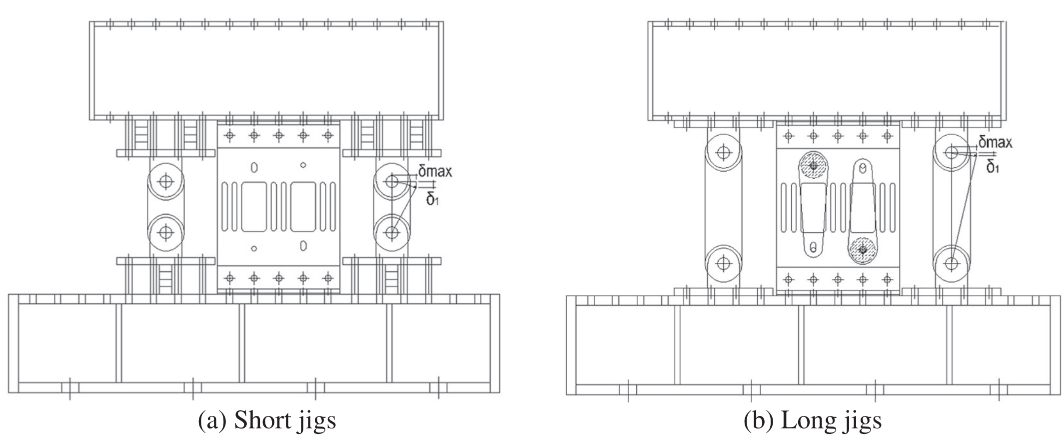

Fig. 6. Types of vertical jigs used for tests.

$$P_y = \left(\frac{n\,\sigma_y t\, b^2}{2\, l_o}\right) + \left(\frac{2\mu N\, Q\, R_m}{L}\right) \tag{3}$$

In this paper the behavior of the hybrid damper is modeled using the 'Rubber Type Seismic Isolator Element' provided in the nonlinear analysis software Perform 3D [21].

3. Configuration and dimension of the hybrid slit-friction damper specimen

The hybrid damper developed in this study consists of a steel slit damper to resist strong earthquakes and friction dampers to dissipate vibration energy caused by small earthquakes or strong winds. The two

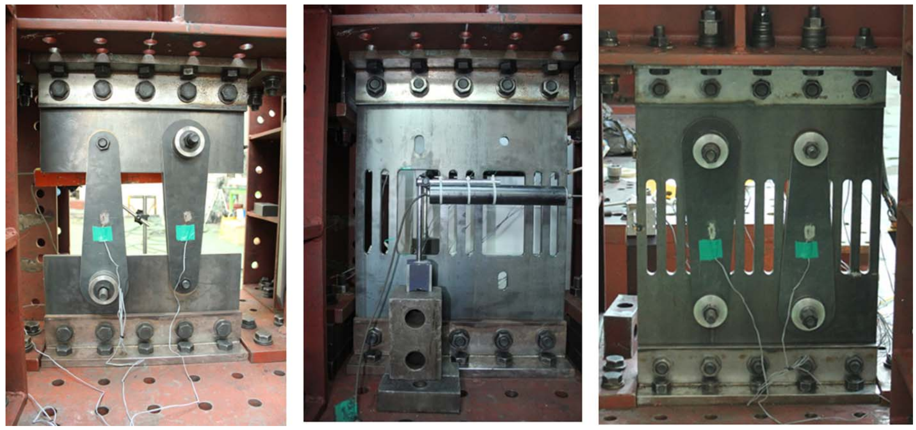

(a) Friction damper (b) Slit damper (c) Hybrid damper

Fig. 7. Test specimens.

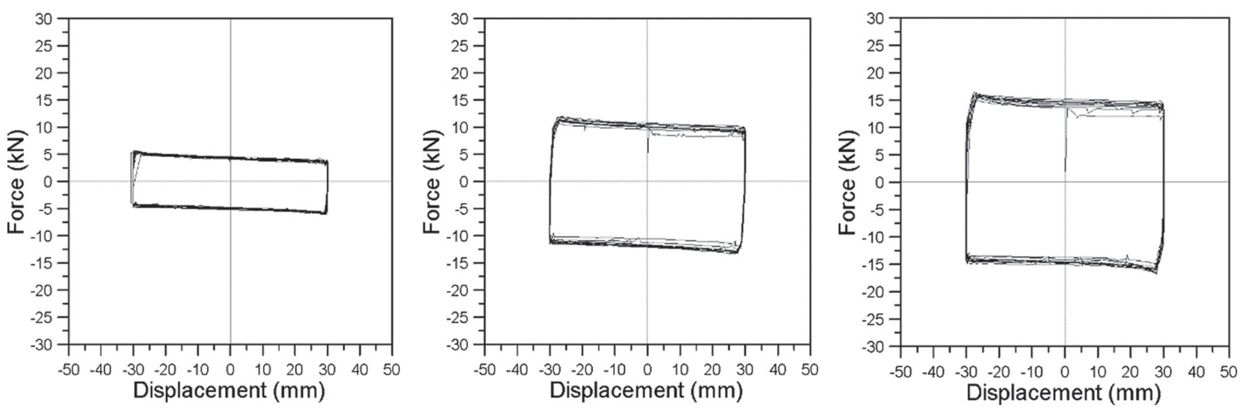

(a) 50 kN (b) 100 kN (c) 150 kN

Fig. 8. Force-displacement curves of friction dampers with different bolt tensions.

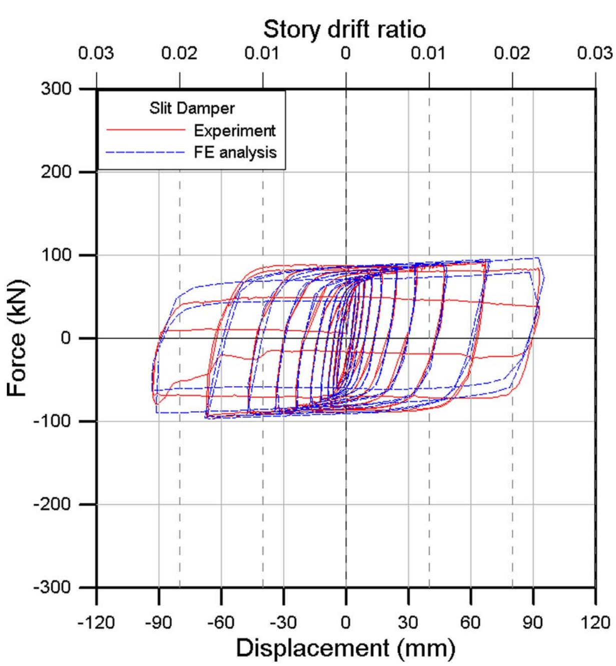

Fig. 9. Hysteresis curves of the slit damper obtained from test and FE analysis.

dampers are connected in parallel as shown in Fig. 1. The overall width and height of the steel plate are 500 mm and 700 mm, respectively. The plate has nine strips: the width (b), thickness (t), and the height (L_o) of each strip are 20 mm, 15 mm, and 200 mm respectively. The circular friction pad with diameter of 100 mm is attached to the slit damper using a steel bar fastened by a high-tension bolt. A 1.0 mm-deep recess is made on the surface of both the slit damper plate and the steel bar to prevent lateral movement of the friction pad and to restrain radial elongation of the pad due to the large compression force applied by the high-tension bolt. To evenly distribute the bearing force induced by the high-tension bolts on the surface of the friction pad, the friction force distribution plates are inserted between the bolt head or the nut and the steel bars. The high-tension bolts used to provide compression force on the friction pads have the tensile strength of 1.0 kN/mm^2 with diameter of 20 mm. At the other end of the steel bar a Teflon-coated washer plate is inserted and the bolt is loosely fastened to reduce friction force to a negligible level.

The hybrid damper is basically a displacement-dependent device which dissipates seismic energy by yielding of steel strips (slit dampers) and by slip of friction pads (friction dampers). The slip of friction pads occurs at small displacement, which makes it effective in resisting small earthquakes and strong wind loads. The slit dampers remain elastic during small earthquakes and are activated at major earthquakes. As the slit dampers yield at in-plane deformation, they have higher strength compared with yield devices such as ADAS [22] and T-ADAS systems [23] which dissipate energy by out of plane yielding.

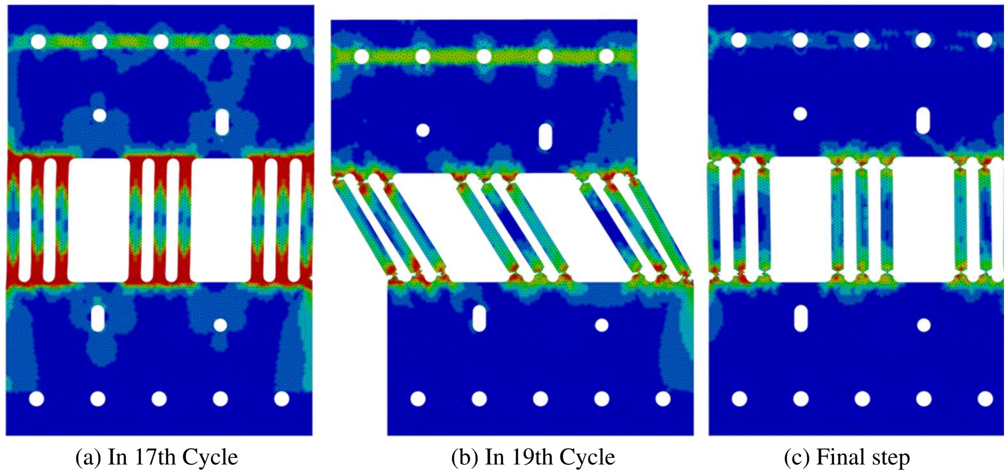

Fig. 10. Stress contour of the slit damper obtained from FE analysis.

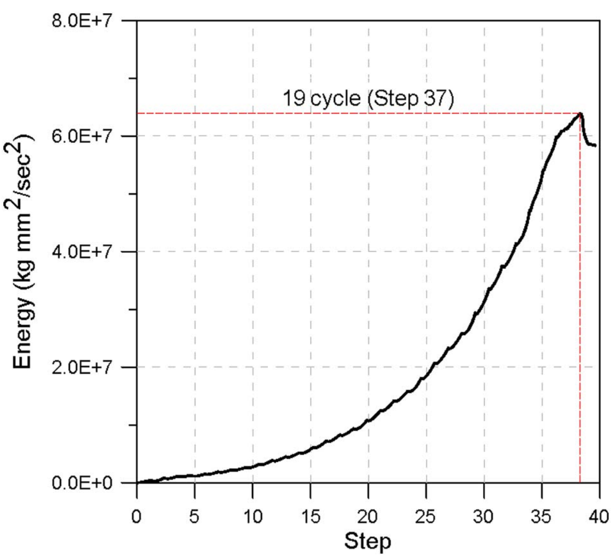

Fig. 11. Time history of internal energy in the slit damper.

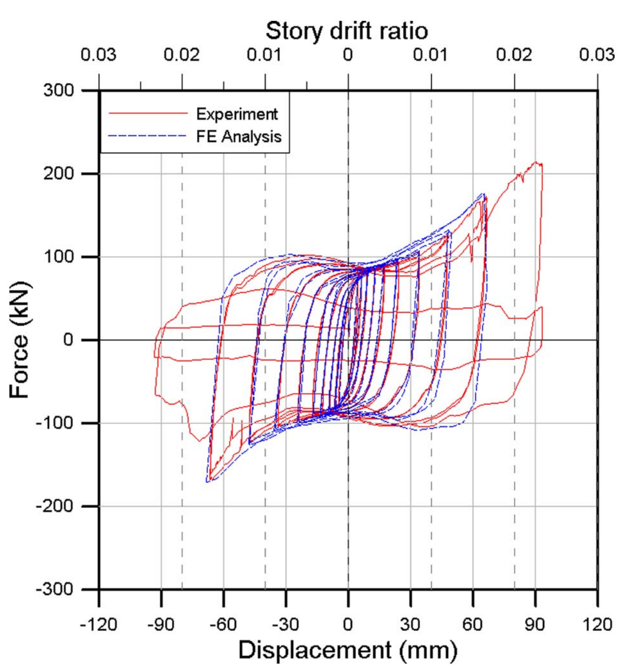

Fig. 12. Hysteresis curves of the hybrid damper obtained from test and FE analysis.

4. FE analysis and loading tests of the test specimens

To finalize the overall configuration of the hybrid dampers and to verify the test results, static implicit finite element analyses are carried out using the finite element analysis software Ls-Dyna [24]. Fig. 2 shows the finite element mesh generation for the slit plate, friction pad, connecting plate, and the high tension bolts modeled by the 8-node hexahedron solid elements using the material keyword of *MAT PIECEWISE LINEAR PLASTICITY. The interface of each element is defined by the keyword *CONTACT AUTOMATIC SURFACE TO SURFACE. The friction coefficient of the friction pad obtained from the experiment is used in the analysis.

To measure the actual yield and ultimate strengths of the steel from which the test specimens are made, coupon tests are performed using a universal testing machine. Fig. 3 shows the stress-strain relationship of the steel obtained from tensile test of three coupons. It can be observed that the mean yield and the ultimate strengths are 325.6 and 376.5 N/mm^2, respectively, which are used in the structural analysis.

Displacement-controlled cyclic tests of the specimens are carried out using a 500 kN hydraulic servo actuator to evaluate their seismic performance. The test specimens consist of a steel slit damper, rotational friction dampers with three different bolt pretensions (50 kN, 100 kN, and 150 kN), and a slit-friction hybrid damper in which the slit and the friction dampers having friction pads with friction coefficient $\mu = 0.30$ are connected in parallel by high-tension bolts with 150 kN pretension. Strain gages are attached on the surface of the strip and the steel bars in the friction dampers. LVDT (linear variable differential transformer) is installed to measure the horizontal displacement at the upper part of the specimens during experiments. The loading protocol for quasi-static cyclic tests specified in the FEMA-461 [25] and depicted in Fig. 4 is followed for tests of the specimens. For the slit and the hybrid dampers the minimum displacement (Δ_o) is determined to be 1.5 mm which corresponds to 0.15% of the inter-story drift in a structure with 3 m story height. After each two cycles of loading, the displacement amplitude is increased to 1.4 times the previous one until the displacement reaches the target displacement of 60 mm which corresponds to 2% of the story height. For friction dampers 10 cycles of harmonic loading is applied in such a way that the maximum displacement of 30 mm is reached at each loading cycle. The setup for cyclic loading test is depicted in Fig. 5. Preliminary finite element analysis shows that tension field is generated at large lateral displacement when vertical displacement of the specimen is restrained. To take into account the effect of tension field on the force-deformation relationship of the test specimens, two types of vertical jigs located at both sides of the specimens are used for test setup as described in Fig. 6; short jigs which allow reduction of specimen height at large lateral

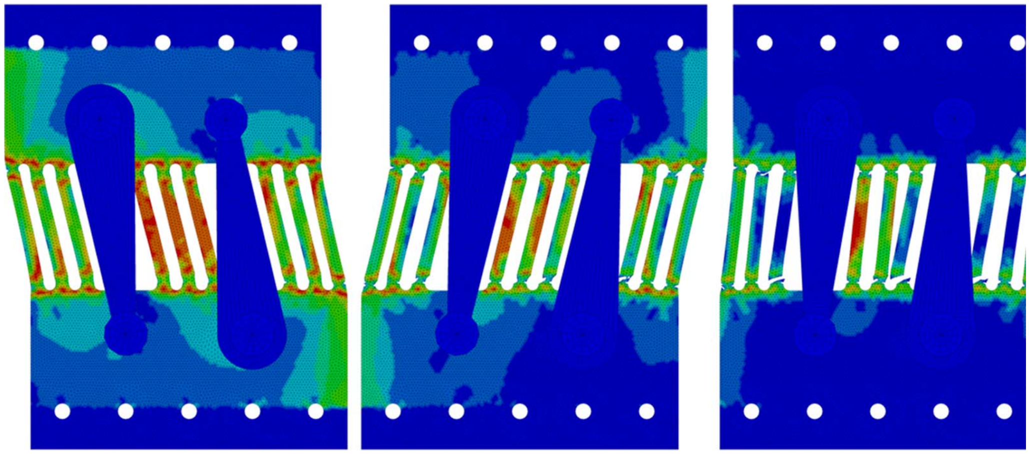

(a) At 16th Cycle (b) At 18th Cycle (c) At final step

Fig. 13. Stress contour of the hybrid damper obtained from FE analysis.

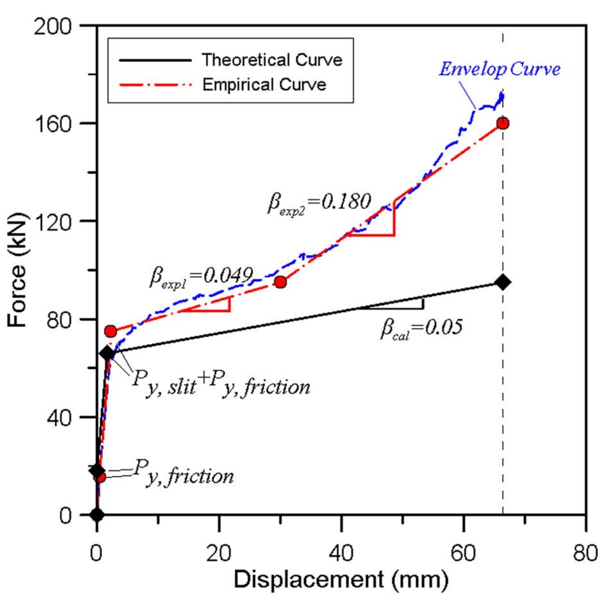

Fig. 14. Idealized force-displacement curve of the hybrid dampers.

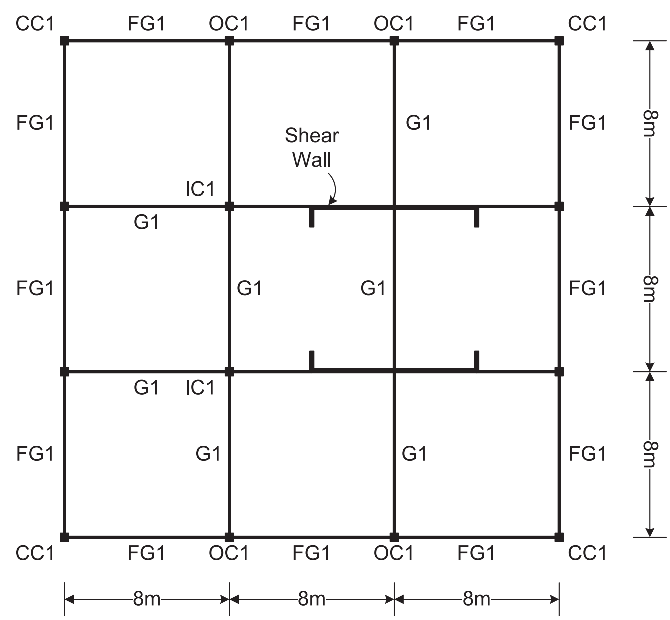

Fig. 15. Structural plan of the analysis model structure.

displacement (Fig. 6(a)) and long jigs which restrains reduction of height at large lateral displacement (Fig. 6(b)). The former is used in the test of the friction dampers and the slit damper, and the latter is used for the hybrid damper.

Fig. 7(a) shows the friction damper installed inside of the strong frame, and Fig. 8 presents the test results with three different bolt pretensions using the loading protocol presented in Fig. 4(a). It is observed that the yield force varies proportionally to the imposed pretension as predicted by Eq. (2). Fig. 7(b) depicts the installation of the slit damper, and Fig. 9 shows the force-displacement relationship of the slit damper obtained from the cyclic loading test and the FE analysis using the loading protocol presented in Fig. 4(b). In Fig. 9 lateral displacement of the damper is also presented as corresponding story drift ratio assuming that the damper is installed in a structure with story height of 4 m. It is observed from both the analysis and the experiment that the slit damper shows stable hysteretic behavior until fracture of slit columns at the 17th loading cycle. At the 19th loading cycle the strength of the damper drops significantly and at the 20th cycle all slit columns fracture. The maximum story drift ratio is slightly over 2% of the 4 m story height, and will be increased to 3% when the story height is reduced to 3 m. Considering the fact that the performance limit state after the seismic retrofit is the maximum drift ratio of 1.5% of the story height, the damper seems to have enough deformation capacity for design level earthquakes.

Fig. 10 shows the stress contours of the slit damper at the selected loading cycles obtained from the finite element analysis. It can be observed in Fig. 10(a) that fracture starts at the bottom end of the right-hand-side slit at the 17th loading cycle; at the 19th cycle most of the slits are fractured at both ends (Fig. 10(b)); and at the final (20th) loading cycle all slits are lightly stress implying that the damper can no longer resist lateral load (Fig. 10(c)). As can be observed in Fig. 10(b), the overall height of the specimen is significantly reduced at large lateral displacement, which is possible due to the use of the short jigs. As a result no tension field is generated in the specimen, which results in force-displacement relationship contributed only from flexural deformation of the strips as observed in Fig. 9. Fig. 11 depicts the time

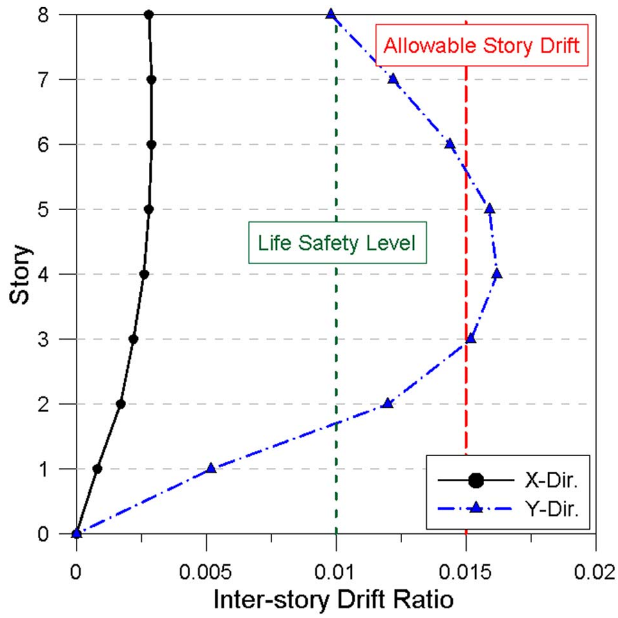

Fig. 16. Inter-story drift ratio of model structure subjected to the design seismic load.

history of the internal energy in the slit damper, where the energy keeps increasing until 19th loading cycle and decreases afterward implying occurrence of failure.

Fig. 12 shows the force-displacement relationship of the hybrid damper depicted in Fig. 7(c), obtained from the cyclic loading test and the FE analysis. It is observed from the test that fracture at a strip occurs first at the 16th loading cycle and strength drops after the 18th cycle. Similar behavior is also observed from the FE analysis and the time history of the internal energy. Fig. 13 shows the stress contours in the steel plate of the hybrid damper at the 16th, 18th, and the 20th loading cycles obtained from the FE analysis. As mentioned previously, long jigs are used in the test of the hybrid damper, which allows little vertical displacement at the large lateral drift as shown in Fig. 6(b). This induce diagonal tension field at large displacement as observed in Fig. 13, which results in further increase in post-yield strength at lateral displacement higher than 30 mm as can be observed in the hysteresis curves presented in Fig. 12. The increase in strength due to formation of tension field in steel hysteretic dampers can also be observed in Whittaker et al. [22].

Based on the hysteresis curve the envelop curve is obtained by connecting the maximum points of the hysteresis curves, which is idealized by a series of linear lines for nonlinear analysis as depicted in Fig. 14. The post-yield stiffness increases from 4.9% to 18% of the initial stiffness due to the formation of tension field. Also shown is the theoretical curve drawn using Eqs. (1a) and (1b) to Eq. (3) with post-yield stiffness of 5% of the initial stiffness, which forms a lower bound compared with the curve obtained based on experimental results. It is observed that the initial stiffness of the specimen computed using Eq. (1a) is 8% higher than the stiffness obtained from the test.

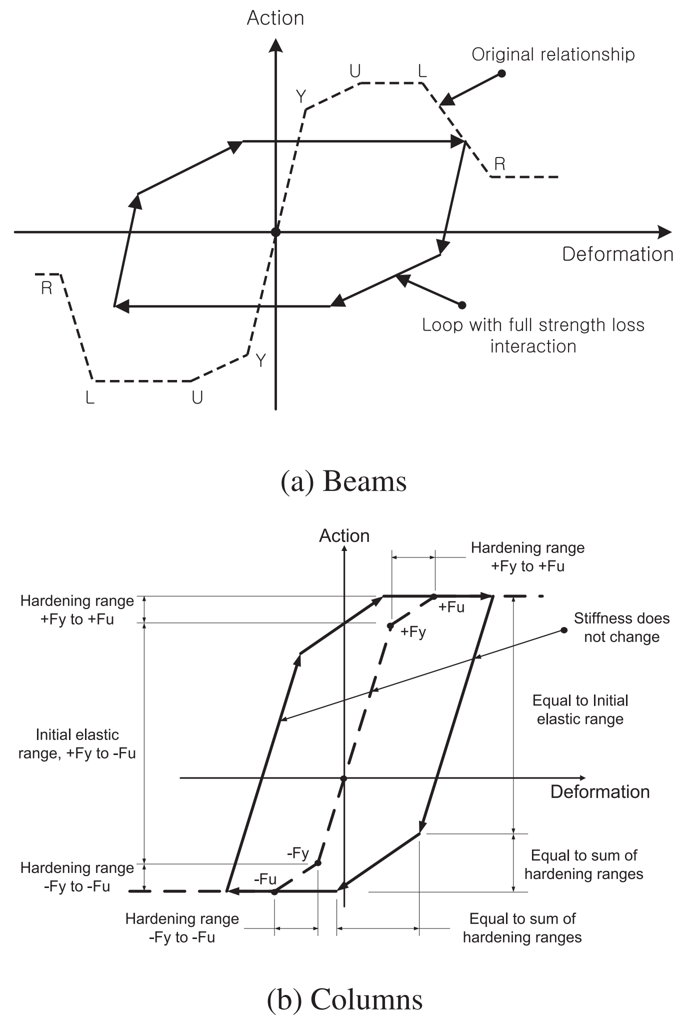

Fig. 18. Hysteresis loops of RC beams and columns.

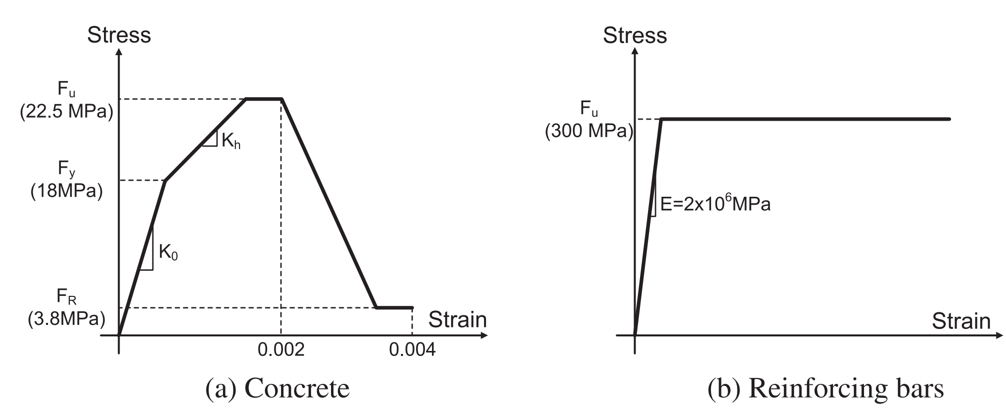

Fig. 17. Nonlinear stress-strain relationship of structural materials.

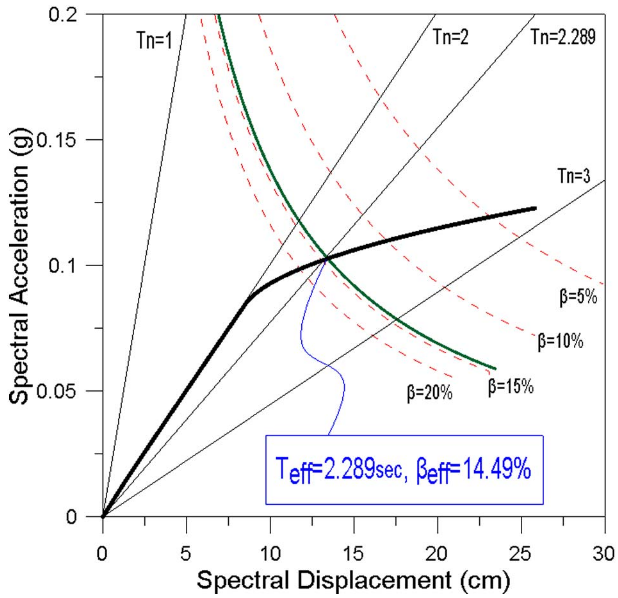

Fig. 19. Performance point of the model structure obtained from capacity-demand diagram.

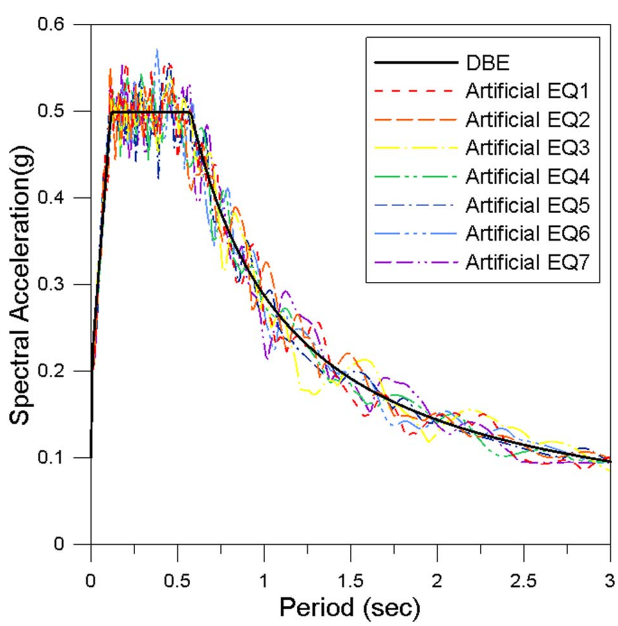

Fig. 20. Design spectrum and the response spectra of the seven artificial earthquake records.

5. Seismic retrofit of a RC structure with hybrid dampers

5.1. Design of analysis model structure

In this section the seismic performance of a structure retrofitted with the hybrid dampers is evaluated to verify the effect of the damper on enhancing seismic load resisting capacity. The analysis model structure is an eight-story reinforced concrete moment frame with core walls as shown in Fig. 15 designed for gravity loads (dead load of 4 kN/m^2 and live load of 3.5 kN/m^2) and wind load with basic wind speed of 30 m per second. The structure has a uniform story height of 4 m. The 20 cm-thick core walls are located along the horizontal (x) axis, which are designed to resist most of the lateral load. The moment frames work as gravity frames in this direction. Along the vertical (y) axis, where no shear wall exists, the moment frames are designed to resist the lateral loads. As the model structure is flexible and large deflection is expected along the vertical axis, p-delta effect is considered in the seismic analysis. In consideration of cracked section, the flexural and the shear stiffness of beams and shear walls are reduced by 50% and 40%, respectively. The flexural stiffness of columns is reduced by 50% or by 70% depending on the level of axial load, and the shear stiffness is reduced by 40%. Using the reduced stiffness of elements, the fundamental periods of the structure turn out to be 0.64 and 2.2 s along the horizontal and the vertical directions, respectively.

Fig. 16 shows the inter-story drifts of the model structure subjected to the design seismic load (S_{DS} = 0.499 g, S_{D1} = 0.287 g). It can be observed that along the horizontal direction the maximum inter-story drift is well within the limit state of 1.5% of the story height, while the maximum value exceeds the limit state along the vertical direction. This study intends to retrofit the model structure using the hybrid dampers so that the maximum inter-story drift satisfies the life safety limit state of 1.0% of the story height when subjected to the design seismic load.

5.2. Determination of the required damping

To determine the required added damping to satisfy the given performance limit state, the capacity spectrum method specified in the ATC-40 [26] is applied. To this end, nonlinear analyses of the model structure is carried out using Perform 3D. The core shear walls are modeled with the Shear Wall fiber elements, whose stress-strain relationship is defined as tri-linear lines as shown in Fig. 17(a) based on the material model of Paulay and Priestley [28] without confinement effect. In the concrete model the ultimate strength is 22.5 MPa at the strain of 0.002, and the residual strength is defined as 20% of the ultimate strength. The ultimate strain is assumed to be 0.004. The reinforcing steel is modeled with bi-linear lines as shown in Fig. 17(b). An over-strength factor of 1.25 is used for both concrete and reinforcing steel. The shear wall elements are modeled using eight fiber elements with 0.3% reinforcement in each fiber. The analysis model for beam elements are composed of two end rotation type moment hinges defined based on ASCE/SEI 41-06 [29]. Nonlinear static pushover analyses of the model structure are carried out using the lateral load proportional to the fundamental mode shapes until the maximum inter-story drift reaches 4% of the story height. Fig. 18 shows the hysteresis loops of the beams and columns used in the dynamic analysis.

Fig. 19 shows the capacity curve of the structure along the vertical axis and the demand curves for various effective damping ratios. The effective period can be obtained using the following formula presented in the ASCE/SEI 41-06:

$$T_{eff} = T_i\sqrt{\frac{K_i}{K_e}} \tag{4}$$

where T_i is the elastic fundamental period, $K_i$is the elastic lateral stiffness, and $K_e$is the effective lateral stiffness of the building obtained from idealized pushover curve. From the performance point of the model structure corresponding to the maximum inter-story drift of 1% of story height, the effective damping ratio (β_{eff}) of 14.5% is obtained. The total amount of the hybrid dampers required for performance-based seismic retrofit is computed using the following equations provided in the ASCE/SEI 41-06:

$$\beta_{eff} = \beta + \frac{\sum_j W_j}{4\pi\, W_k} \tag{5}$$

$$W_k = \frac{1}{2}\sum_i F_i\delta_i \tag{6}$$

where β is the inherent damping of the system equal to 0.05, W_j is the work done by device j during one complete cycle corresponding to

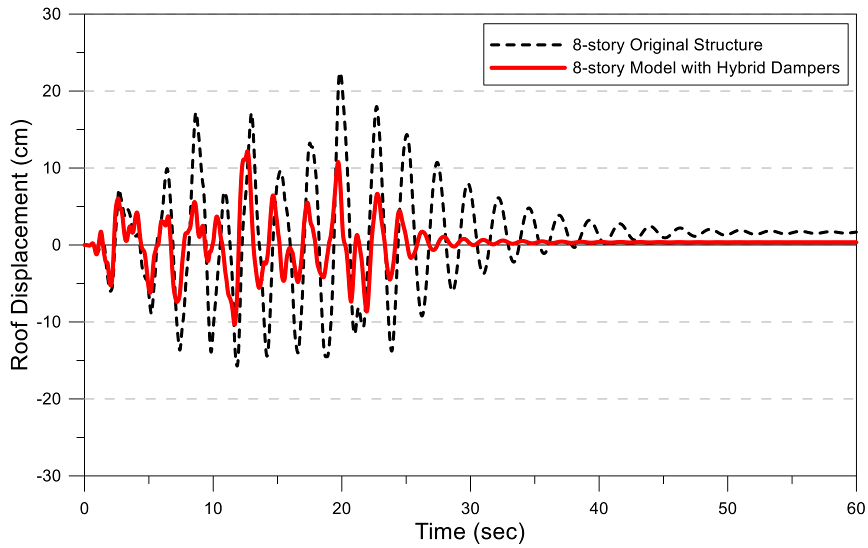

(a) Artificial earthquake-1

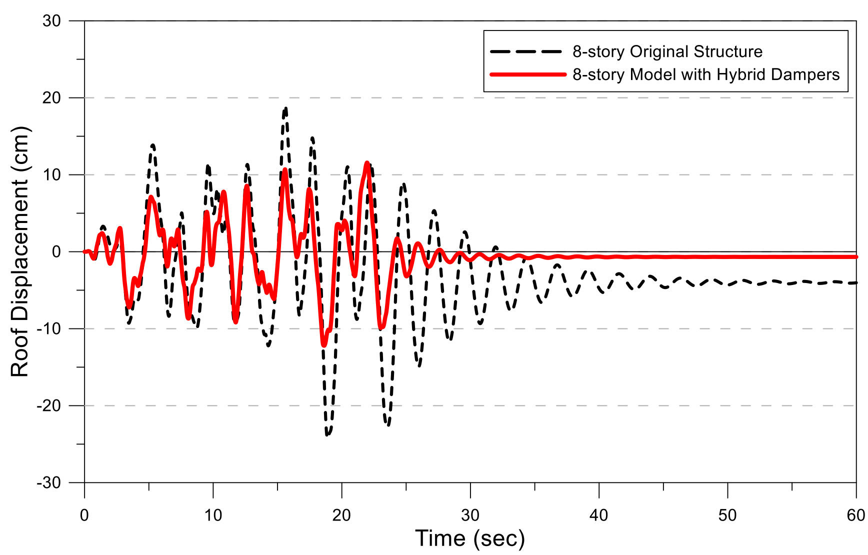

(b) Artificial earthquake-3

Fig. 21. Roof displacement time history of the model structure without and with hybrid dampers.

the floor displacement δ_i, F_i is the design seismic story force corresponding to 2/3 of the maximum considered earthquake, and W_k is the maximum strain energy in the frame. From the above equation the required yield force of the hybrid damper at each story is computed using known lateral force and displacement assuming that the damper force is distributed proportionally to the inter-story drift under design seismic load. As many assumptions and simplifications are involved in the above process, the required damping obtained by the above process may not be an optimum value. However it may be used as the first trial value for required damping, which can be refined through iteration.

5.3. Nonlinear dynamic analysis results

To validate the effect of the hybrid dampers designed based on Eq. (5) on the mitigation of seismic response, nonlinear dynamic analyses are carried out using the seven artificial earthquake records generated based the design spectrum (S_{DS} = 0.499 g, S_{D1} = 0.287 g). Fig. 20 depicts the design spectrum and the response spectra of the seven artificial earthquakes. The nonlinear behavior of the hybrid damper is represented by the idealized curve shown in Fig. 14. Fig. 21 shows the roof displacement time histories for two selected earthquakes (EQ-1 and EQ-3), where it can be observed that, after installation of the hybrid dampers following the process described above, both the maximum and the residual displacement decrease. Fig. 22 plots the maximum and the mean inter-story drifts of the model structures obtained from the nonlinear dynamic analyses using the seven artificial earthquakes. It can be observed that both the maximum and the mean inter-story drifts are restrained well within the given target drift of 1% of the story height. Although not tried in this study, the total amount of the dampers may be further optimized by a few more iteration. Fig. 23 shows the hysteresis curve of the hybrid damper located in the 6th story of the model structure when it is subjected to the record EQ-7 (PGA = 0.199 g). It can be observed that the hybrid damper shows stable hysteretic behavior under the earthquake load. Fig. 24 depicts

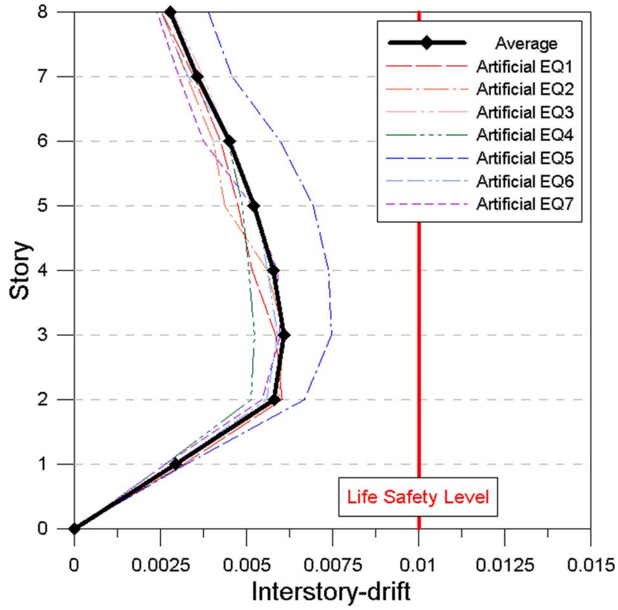

Fig. 22. Inter-story drifts of the model structure for the 7 artificial earthquakes.

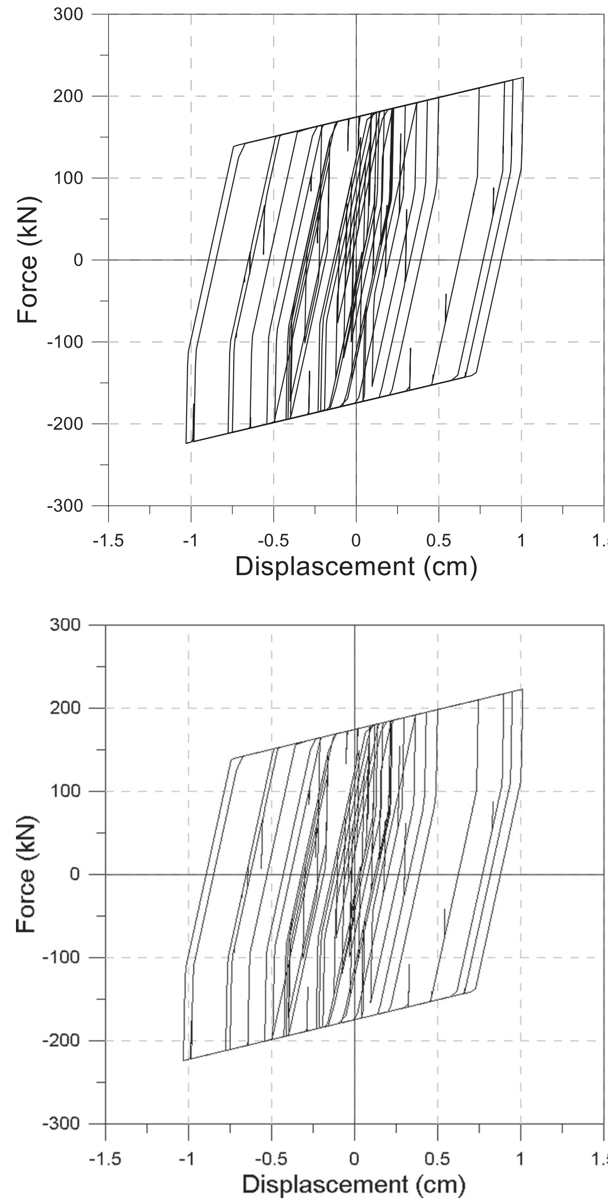

Fig. 23. Hysteresis loop of hybrid damper at the 6th story (Artificial record EQ7).

the hysteretic energy time histories in the model structure subjected to the EQ-7 earthquake. It is observed that 84% of the seismic energy is dissipated by inelastic deformation of beams and the remaining 16% is dissipated by columns before the retrofit, whereas most of the hysteretic energy is dissipated by the dampers in the retrofitted structure.

5.4. Evaluation of the seismic fragility

Fragility analysis is generally used to estimate the probability of a structure to reach a given damage state. The seismic fragility is described by the conditional probability that the structural capacity, *C*, fails to resist the structural demand, *D*, given the seismic intensity hazard, *SI*, and is modeled by a lognormal cumulative distribution function as follows [27]:

$$P[C < D \mid SI = x] = 1 - \Phi\left[\frac{\ln(\widehat{C}/\widehat{D})}{\sqrt{\beta_{D|SI}{}^2 + \beta_C{}^2 + \beta_M{}^2}}\right] \tag{7}$$

where $\Phi[\cdot]=$ standard normal probability integral, $\widehat{C}=$ median structural capacity associated with the limit state, $\widehat{D}=$ median structural demand, $\beta_{D|SI}=$ uncertainty in *D*, $\beta_C=$ uncertainty in C, and $\beta_M=$ modeling uncertainty. FEMA P695 [30] provides β_{TOT}, the total system collapse uncertainty, for the uncertainty in the normal probability integral function Φ in Eq. (7) based on the record-to-record uncertainty, design requirements related uncertainty, test data-related uncertainty, and the modeling uncertainty. In this study the total system collapse uncertainty, β_{TOT}, provided in the FEMA P695 (2009) is used for the uncertainty in the lognormal cumulative distribution function. The design requirement related uncertainty and the test data-related uncertainty are assumed to be 'Good' and 'Fair', respectively, and the modeling uncertainty is assumed to be 'Good'. These assumptions leads to the total system collapse uncertainty equal to 0.6.

Nonlinear incremental dynamic analyses of the prototype and the damped structures are conducted using the 22 pairs of the far field ground motions provided by the PEER NGA Database [31] to establish the median and the standard deviation of the collapse capacity of each analysis model. Fig. 25 depicts the spectral acceleration vs. maximum inter-story drift ratio curves obtained by incremental dynamic analyses of the prototype structure and the structure with hybrid dampers. It can be observed that, for a given spectral acceleration, the inter-story drift of the model structure decreases after retrofit with the dampers. Based on the incremental dynamic analysis results the probability of reaching given limit states is computed for the four damage states defined in the HAZUS [32], which are Slight, Moderate, Extensive, and Complete damages. Table 1 shows the inter-story drift ratio corresponding to each damage index used in the fragility analysis. Fig. 26 depicts the fragility curves of the model structures for the four limit states. The horizontal line at the middle of the figure represents the 50% probability of reaching the limit states and the vertical line indicates the spectral acceleration corresponding to the design seismic load, which is 0.13 g and 0.19 g for the original and the retrofitted structure, respectively. It can be observed that, after the retrofit with the hybrid dampers, the spectral acceleration at the median probability of reaching each limit state increases by 0.121 g, 0.124 g, 0.154 g, and 0.269 g for the Slight, Moderate, Extensive, and the Complete damage states, respectively. It also can be noticed that the probability of reaching each limit state at the design level spectral acceleration decreases from 71%, 52%, 35%, and 19% to 42%, 32%, 19%, and 6% for the four given limit states,

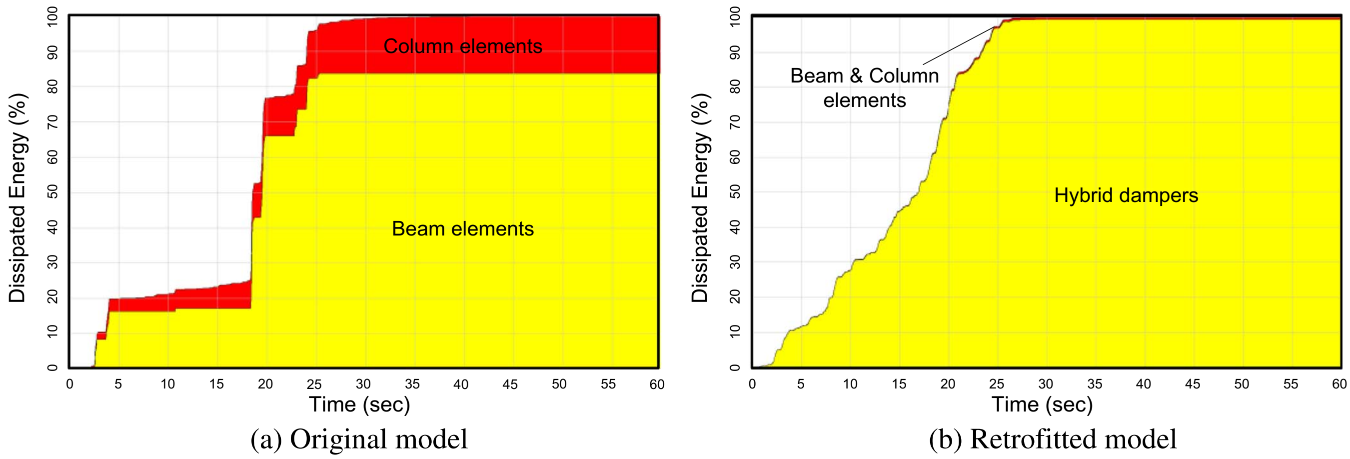

Fig. 24. Time history of dissipated hysteretic energy in the model structure subjected to the EQ7 earthquake.

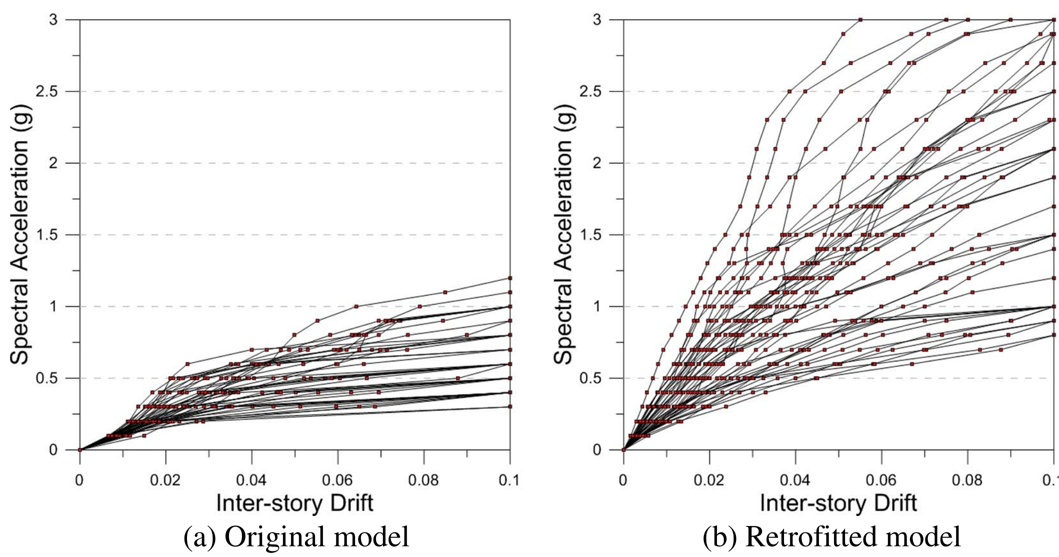

Fig. 25. Incremental dynamic analysis results of the model structures.

Table 1
Damage index and corresponding inter-story drift ratio used in the fragility analysis.

	Inter-story drift ratio (%)			
	Slight	Moderate	Extensive	Complete
Original structure	0.75	1.08	1.34	2.34
Retrofitted structure	0.68	0.94	1.21	2.39

respectively. These observations confirm that after installation of the hybrid dampers the decrease in the probability of reaching the Complete damage state is the most significant.

6. Conclusions

In this paper a new hybrid damper composed of a steel slit damper and rotational friction dampers was proposed and its effectiveness was investigated by both cyclic loading tests and finite element analyses. The hybrid dampers were applied to seismic retrofit of a reinforced concrete model structure to validate their effectiveness. The seismic performance of the model structure retrofitted with the hybrid dampers was evaluated using the nonlinear model of the dampers obtained from the experiment. Fragility analysis was also conducted to estimate the probability of the model structure to reach each damage state.

Both the analysis and the test results showed that the hybrid dampers were effective in dissipating seismic energy through stable hysteretic behavior throughout the given loading history. It was noticed that when vertical deflection of the specimen was restrained the post-yield stiffness increased due to the generation of tension field at large displacement. Similar behavior was observed in the finite element analysis results. The hybrid dampers were used for seismic retrofit of a reinforced concrete structure, and the maximum inter-story drifts of the retrofitted structure averaged over the seven nonlinear analysis results satisfied the given target point. The fragility analysis of the structure showed that the decrease in the probability of reaching the Complete damage state is the most significant after the seismic retrofit.

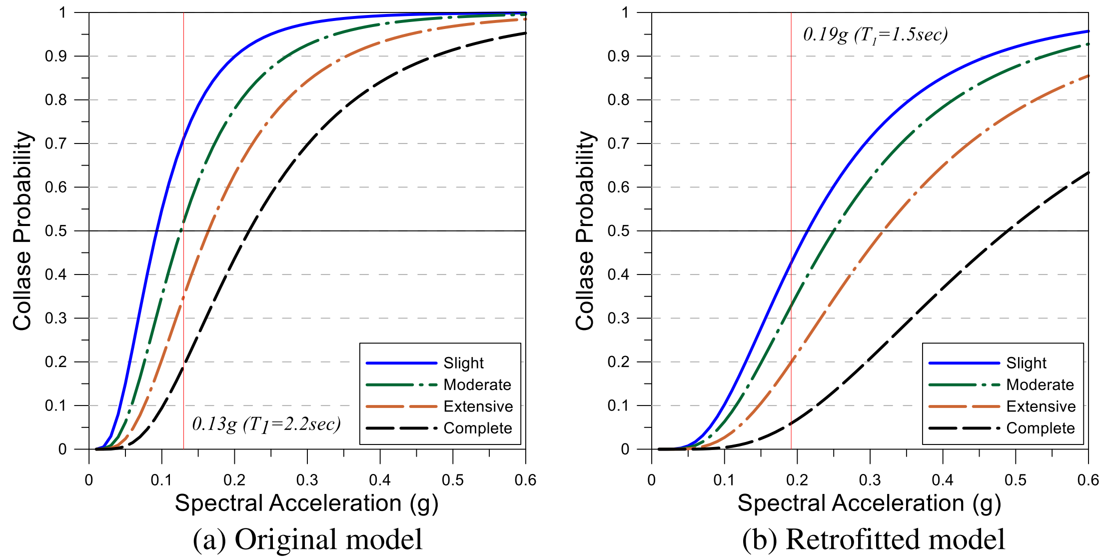

Fig. 26. Fragility curves of the model structures.

Acknowledgement

This research was supported by the Ministry of Trade, Industry and Energy (MOTIE) and Korea Institute for Advancement of Technology (KIAT) through the International Cooperative R & D program (N043100016).

References

[1] C. Xia, R.D. Hanson, Influence of ADAS element parameters on building seismic response, J. Struct. Eng. 118 (7) (1992) 1903–1918 http://ascelibrary.org/doi/pdf/10.1061/(ASCE)0733-9445(1992)118%3A7(1903.
[2] A. Watanabe, Y. Hitomi, E. Saeki, A. Wada, M. Fujimoto, Properties of brace encased in buckling-restraining concrete and steel tube, Proceedings of Ninth World Conference on Earthquake Engineering, 4 1988, pp. 719–724 http://www.akira-wada.com/paper/conference/WCEE1988-6.pdf.
[3] R.W. Chan, F. Albermani, Experimental study of steel slit damper for passive energy dissipation, Eng. Struct. 30 (4) (2008) 1058–1066, http://dx.doi.org/10.1016/j.engstruct.2007.07.005.
[4] J. Kim, J. Jeong, Seismic retrofit of asymmetric structures using steel plate slit dampers, J. Constr. Steel Res. 120 (2016) 232–244.
[5] J. Hu, Investigation on the cyclic response of superelastic shape memory alloy (SMA) slit damper devices simulated by quasi-static finite element (FE) analyses, Materials 7 (2014) 1122–1141, http://dx.doi.org/10.3390/ma7021122.
[6] I.H. Mualla, B. Belev, Performance of steel frames with a new friction damper device under earthquake excitation, Eng. Struct. 24 (3) (2002) 365–371, http://dx.doi.org/10.1016/S0141-0296(01)00102-X.
[7] J. Kim, H. Choi, K. Min, Use of rotational friction dampers to enhance seismic and progressive collapse resisting capacity of structures, Struct. Design Tall Spec. Build. 20 (4) (2011) 515–537.
[8] C.C. Patel, R.S. Jangid, Dynamic response of adjacent structures connected by friction dampers, Earthq. Struct. 2 (2) (2011) 149–169, http://dx.doi.org/10.12989/eas.2011.2.2.149.
[9] N. Kaur, V.A. Matsagar, A.K. Nagpa, Earthquake response of mid-rise to high-rise buildings with friction dampers, Int. J. High-Rise Build. 1 (4) (2012) 311–332.
[10] C.H. Lee, J. Ryu, J. Oh, C.H. Yoo, Y.K. Ju, Friction between a new low-steel composite material and milled steel for SAFE dampers, Eng. Struct. 122 (2016) 279–295.
[11] J. Kim, S. Kim, Performance-based seismic design of staggered truss frames with friction dampers, Thin-Walled Struct. 17 (1) (2017) 197–209.
[12] W.S. Pong, C.S. Tsai, G.C. Lee, Seismic Performance of High-Rise Building Frames with Added Energy-absorbing Devices (NCEER-94-0016), National Center for Earthquake Engineering Research, Red Jacket Quadrangle, Buffalo, NY, 1994.
[13] K. Uetani, M. Tsuji, I. Takewaki, Application of an optimum design method to practical building frames with viscous dampers and hysteretic dampers, Eng. Struct. 25 (5) (2003) 579–592, http://dx.doi.org/10.1016/S0141-0296(02)00168-2.
[14] J.D. Marshall, F.A. Charney, Seismic response of steel frame structures with hybrid passive control systems, Earthq. Eng. Struct. Dyn. 41 (4) (2012) 715–733, http://dx.doi.org/10.1002/eqe.1153.
[15] Y. Murakami, K. Noshi, K. Fujita, M. Tsuji, I. Takewaki, Simultaneous optimal damper placement using oil, hysteretic and inertial mass dampers, Earthq. Struct. 5 (3) (2013) 261–276, http://dx.doi.org/10.12989/eas.2013.5.3.261.
[16] E. Asadi, R. Ribeiro, M.B. Khamesee, A. Khajepour, A new adaptive hybrid electromagnetic damper: modeling, optimization, and experiment, Smart Mater. Struct. 24 (2015), http://dx.doi.org/10.1088/0964-1726/24/7/075003.
[17] D. Wang, T.K.T. Tse, Y. Zhoua, Q. Li, Structural performance and cost analysis of wind-induced vibration control schemes for a real super-tall building, Struct. Infrastruct. Eng. 11 (8) (2015) 990–1011, http://dx.doi.org/10.1080/15732479.2014.925941.
[18] J. Lee, J. Kim, Seismic performance evaluation of moment frames with slit-friction hybrid dampers, Earthq. Struct. 9 (6) (2015) 1291–1311.
[19] J. Kim, H. Shin, Seismic loss assessment of a structure retrofitted with slit-friction hybrid dampers, Eng. Struct. 130 (2017) 336–350.
[20] Damptech, http://www.damptech.com/downloads.html, (2017).
[21] Perform 3D, Computer and Structures. Inc., Berkeley, CA, 2015.
[22] A.S. Whittaker, V.V. Bertero, C.L. Thompson, L.J. Alonso, Seismic testing of steel plate energy dissipation devices, Earthquake Spectra 7 (4) (1991) 563–604, http://dx.doi.org/10.1193/1.1585644.
[23] C.S. Tsai, K.C. Chen, C.S. Chen, Seismic resistibility of high-rise buildings with combined velocity-dependent and velocity-independent devices, ASME-PUBLICATIONS-PVP 366 (1998) 103–110 https://getinfo.de/en/search/id/BLCP%3ACN026985900/.
[24] LS-DYNA®, (971) [Computer Software], Livemore Software Technology Corporation, Livemore, Ca, 2006.
[25] FEMA, Prestandard, Interim Testing Protocols for Determining the Seismic Performance Characteristics of Structural and Nonstructural Components (FEMA 461), Federal Emergency Management Agency, Washington, DC, 2007.
[26] ATC, Seismic Evaluation and Retrofit of Concrete Buildings (Report ATC 40), Applied Technology Council, Redwood City, CA, 1996.
[27] O.C. Celik, B.R. Ellingwood, Seismic risk assessment of gravity load designed reinforced concrete frames subjected to Mid-America ground motions, J. Struct. Eng. 135 (4) (2009) 414–424, http://dx.doi.org/10.1061/(ASCE)0733-9445(2009)135:4(414).
[28] T. Paulay, M.J.N. Priestley, Seismic design of reinforced concrete and masonry building, John Wiley & Sons, Inc, 1992.
[29] ASCE 41-06, Seismic Rehabilitation of Existing Buildings, American Society of Civil Engineers, Virginia(USA), 2007.
[30] FEMA P695, Quantification of Building Seismic Performance Factors, Federal Emergency Management Agency, Washington (DC, USA), 2009.
[31] PEER NGA Database, Pacific Earthquake Engineering Research Center, University of California, Berkeley, U.S.A, 2017 http://peer.berkeley.edu/nga.
[32] HAZUS-MH 2.1, Technical Manual, Federal Emergency Management Agency, Washington (DC, USA), 2010.